



Lagrangian-based numerical investigation of aerodynamic performance of an oscillating foil

Mengjie Zhang¹ · Qin Wu^{1,2} · Biao Huang¹ · Guoyu Wang¹

Received: 26 December 2017 / Accepted: 12 April 2018 / Published online: 23 June 2018

© The Chinese Society of Theoretical and Applied Mechanics; Institute of Mechanics, Chinese Academy of Sciences and Springer-Verlag GmbH Germany, part of Springer Nature 2018

Abstract

The dynamic stall problem for blades is related to the general performance of wind turbines, where a varying flow field is introduced with a rapid change of the effective angle of attack (AOA). The objective of this work is to study the aerodynamic performance of a sinusoidally oscillating NACA0012 airfoil. The coupled $k-\omega$ Menter's shear stress transport (SST) turbulence model and $\gamma-Re_\theta$ transition model were used for turbulence closure. Lagrangian coherent structures (LCS) were utilized to analyze the dynamic behavior of the flow structures. The computational results were supported by the experiments. The results indicated that this numerical method can well describe the dynamic stall process. For the case with reduced frequency $K = 0.1$, the lift and drag coefficients increase constantly with increasing angle prior to dynamic stall. When the AOA reaches the stall angle, the lift and drag coefficients decline suddenly due to the interplay between the first leading- and trailing-edge vortex. With further increase of the AOA, both the lift and drag coefficients experience a secondary rise and fall process because of formation and shedding of the secondary vortex. The results also reveal that the dynamic behavior of the flow structures can be effectively identified using the finite-time Lyapunov exponent (FTLE) field. The influence of the reduced frequency on the flow structures and energy extraction efficiency in the dynamic stall process is further discussed. When the reduced frequency increases, the dynamic stall is delayed and the total energy extraction efficiency is enhanced. With $K = 0.05$, the amplitude of the dynamic coefficients fluctuates more significantly in the poststall process than in the case of $K = 0.1$.

Keywords Oscillating foil · Dynamic stall · Lagrangian coherent structures · Computational fluid dynamics (CFD)

List of symbols

μ	Dynamic viscosity (kg/m·s)
u_i	Velocity in the i -th direction (m/s)
x	Position (m)
k	Turbulent kinetic energy (m^2/s^2)
ω	Specific turbulent dissipation rate (1/s)
Re	Reynolds number
w	Angular velocity (1/s)
δ	Lyapunov exponent
ω_z	z -vorticity (1/s)
Q	Second invariant of velocity gradient tensor ($1/\text{s}^2$)

Δt	Time step (s)
$M(t)$	Torque (N·m)
T	Time period of one cycle (s)
$w_p(t)$	Pitching angular velocity (1/s)
ρ	Density (kg/m^3)

1 Introduction

With the development of renewable energy sources, wind energy has attracted much attention as a clean, rich, and widely distributed resource [1–3]. As an important wind energy capture device, wind turbines have been widely applied [4–6]. However, the dynamic stall problem is closely related to the general performance of wind turbine systems in a varying flow field, such as yawed operation, sheared inflow, gust conditions, etc., which are accompanied by a rapid change of the effective angle of attack [7–11]. Hence, it

✉ Qin Wu
wuqin919@bit.edu.cn

¹ School of Mechanical Engineering, Beijing Institute of Technology, 100081 Beijing, China

² Department of Thermal Engineering, Tsinghua University, Beijing 100084, China

is of significant importance to understand the dynamic interactions between transient wing motion and unsteady flow structures. Moreover, as one of the primary flow energy conversion technologies, improved understanding of dynamic stall characteristics will help development of oscillating wing systems to enhance the energy harvesting performance of wind or hydro energy.

Many experimental and numerical studies have been carried out on the aerodynamic performance of oscillating foils [12–17]. Ferreira et al. [18] used particle image velocimetry (PIV) to visualize the transient flow in the operational regime. The results illustrated that the flow pattern is dependent not only on the magnitude of the angle of attack (AOA) but also on the transportation and interaction of the shedding vorticity. Wernert et al. [19] used laser-sheet visualization and PIV to investigate the unsteady flow around a pitching airfoil. They found that the dynamic stall process can be categorized into four stages: (1) attached flow, (2) development of the leading-edge vortex (LEV), (3) poststall vortex shedding, (4) flow reattachment. Lee and Gerontakos [20] applied smoke flow visualization and hot-film sensors to investigate the transient flow structures and dynamic stall characteristics of an oscillating NACA0012 airfoil. They illustrated that the boundary-layer transition and dynamic stall point were delayed with increase of the reduced frequency. This conclusion has also been proved experimentally by Carr [21] and Ekaterinaris and Platzer [22]. Simpson et al. [23] experimentally studied the unsteady flow around a sinusoidal heaving and pitching foil, focusing on the influence of the maximum AOA, Strouhal number, and aspect ratio on the energy extraction. The results revealed hydrodynamic efficiency of $43\% \pm 3\%$ with maximum AOA of 34.37° , Strouhal number of 0.4, and aspect ratio of 7.9.

With the development of computing equipment and techniques, much attention has been paid to computational fluid dynamics to better investigate dynamic stall characteristics [24–28]. Hang et al. [4] numerically investigated the performance of offshore floating vertical-axis wind turbines subjected to pitch motion. The results indicated that the power output of the turbines and the range of aerodynamic force variations were enlarged. The transient flow of an oscillating hydrofoil at different pitching rates was studied numerically by Huang et al. [7,29]. The results revealed that the pitching velocity had an important effect on the hydrodynamic characteristics. The energy harvesting performance of a fully activated flapping foil under wind gust conditions was studied by Chen et al. [30]. Compared with the uniform flow condition, the energy harvesting efficiency was higher. Energy extraction efficiency with pitching motion was also investigated by Teng et al. [31]; the results showed that nonsinusoidal pitch-

ing motion had a negative effect on the harvesting efficiency.

Although much work has been carried out on the aerodynamic performance of oscillating wind turbine blades [32–36], significant uncertainty still exists regarding the influence of unsteady flow features. The effect of the dynamic stall phenomenon on energy harvesting still cannot be explained clearly, and the influence of the reduced frequency on the flow evolution and energy harvester efficiency still requires further investigation. The objective of the work presented herein is to analyze the flow vortex structures around an oscillating foil using a Lagrangian-based numerical method, and provide further insight into the interplay between the unsteady flow, oscillatory motion of the foil, and aerodynamic performance. The numerical models are described in Sect. 2, followed by a summary of the numerical setup in Sect. 3. In Sect. 4, detailed analysis of the aerodynamic performance and flow structures is presented. Finally, conclusions are drawn in Sect. 5.

2 Numerical model

2.1 Basic governing equations

The flow field was simulated by solving the unsteady Reynolds-averaged Navier–Stokes (URANS) equations, with the continuity and momentum equations listed below:

$$\frac{\partial u_j}{\partial x_j} = 0, \quad (1)$$

$$\rho \left[\frac{\partial u_i}{\partial t} + \frac{\partial (u_i u_j)}{\partial x_j} \right] = -\frac{\partial p}{\partial x_i} + \frac{\partial}{\partial x_j} \left(\mu \frac{\partial u_i}{\partial x_j} \right), \quad (2)$$

where ρ is the fluid density (all flow conditions in this study being incompressible), t is time, u is the velocity, x is the coordinate, p is the pressure, μ is the fluid viscosity, and subscripts i and j denote the directions of the Cartesian coordinates.

2.2 Turbulence model

The simulation solved the URANS equations by applying the revised k – ω SST turbulence model, which couples the k – ω shear stress transport (SST) turbulence model [37] and the γ – Re_θ transition model [38–40]:

$$\begin{aligned} \frac{\partial (\rho k)}{\partial t} + \frac{\partial (\rho u_j k)}{\partial x_j} &= \tilde{P}_k - \tilde{D}_k \\ &+ \frac{\partial}{\partial x_j} \left[(\mu + \sigma_k \mu_t) \frac{\partial k}{\partial x_j} \right], \end{aligned} \quad (3)$$

$$\begin{aligned} \frac{\partial(\rho\omega)}{\partial t} + \frac{\partial(\rho U_j \omega)}{\partial x_j} &= C_\omega P_\omega - \beta_\omega \rho \omega^2 \\ &+ \frac{\partial}{\partial x_i} \left[\left(\mu + \frac{\mu_t}{\sigma_k} \right) \frac{\partial \omega}{\partial x_i} \right] \\ &+ 2\rho(1 - F_1)\sigma_\omega 2 \frac{1}{\omega} \frac{\partial k}{\partial x_i} \frac{\partial \omega}{\partial x_i}, \end{aligned} \tag{4}$$

where k and ω are the turbulent kinetic energy and specific turbulent dissipation, respectively, F_1 is the blending function, and \tilde{P}_k and \tilde{D}_k are the revised production and destruction term, respectively, defined as

$$\tilde{P}_k = \gamma_{\text{eff}} P_k, \tag{5}$$

$$\tilde{D}_k = \min[\max(\gamma_{\text{eff}}, 0.1), 1.0] D_k, \tag{6}$$

where P_k is the original production terms, D_k is the original destruction term, and γ_{eff} is the revised coefficient.

2.3 Lagrangian coherent structures

In contrast to the Eulerian approach, the Lagrangian approach considers the fluid flow as a particle-based dynamic system [41]. To characterize the separation rate of infinitely close trajectories, the Lyapunov exponent is defined as

$$\sigma = \lim_{t \rightarrow \infty} \left(\frac{1}{t} \ln \frac{|\delta x(x_0, t)|}{|\delta x_0|} \right), \tag{7}$$

where t is time and x_0 is an arbitrary point in the dynamical system. Based on the Cauchy–Green deformation tensor, the separation rate can be obtained as

$$\Delta_{t_0}^{T_{LE}}(x_0) = \left[\frac{\partial x(t_0 + T_{LE}; t_0, x_0)}{\partial x_0} \right]^T \frac{\partial x(t + T_{LE}; t_0, x_0)}{\partial x_0}, \tag{8}$$

where T_{LE} is the time interval and $x(t_0 + T_{LE}; t_0, x_0)$ is the new position of point x_0 after T_{LE} . Then, the finite-time Lyapunov exponent (FTLE) during the time interval T_{LE} is defined as

$$\sigma_{t_0}^{T_{LE}}(x_0) = \frac{1}{|T_{LE}|} \ln \sqrt{\lambda_{\max} \left[\Delta_{t_0}^{T_{LE}}(x_0) \right]}, \tag{9}$$

where $\lambda_{\max} \left[\Delta_{t_0}^{T_{LE}}(x_0) \right]$ is the maximum eigenvalue of the Cauchy–Green deformation tensor. Based on the FTLE field, the Lagrangian coherent structures (LCS) can be obtained from the ridges of the FTLE field, and it has been proven that this is useful to capture the vortex boundary [42,43].

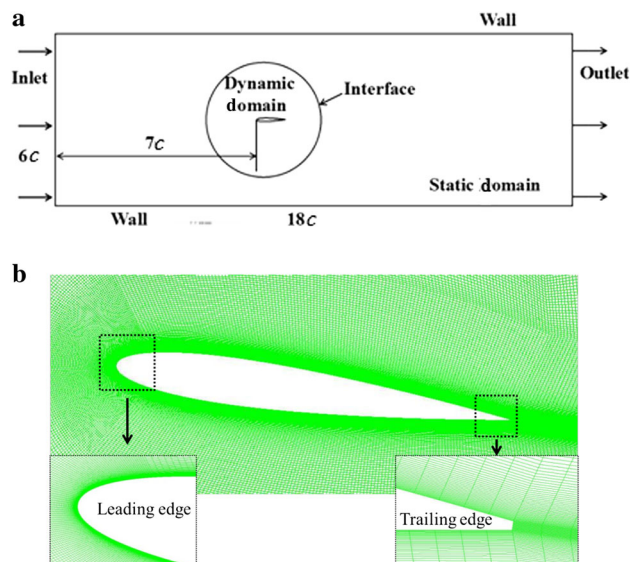


Fig. 1 2D fluid mesh and boundary conditions: **a** simulation domain and boundary conditions, **b** mesh distribution

3 Numerical setup and description

3.1 Numerical setup

In this study, the NACA0012 airfoil was adopted with chord length of $c = 0.15$ m. According to the experimental setup [20], the computational domain and boundary conditions are presented in Fig. 1a, containing two domains connected by a sliding interface. The rectangular static domain has length of $18c$ and height of $6c$, while the circular dynamic domain has diameter of $4c$. The interaction between the static and dynamic domains is controlled using a CFX expression language (CEL) subroutine. The foil was located $7c$ from the inlet. The pitching motion of the foil was simulated by setting the pitching motion of the dynamic domain, i.e., the cylindrical region around the 1/4-chord of the foil. The dynamic domain is moving as a whole, while the grids of the dynamic domain remain invariant. The inlet velocity and outlet pressure are set, and nonslip wall conditions are applied to the upper and lower flow boundary, as well as the foil surface. Figure 1b shows the mesh distribution as well as the refined grids around the foil. A total of 450 nodes are placed in the boundary layer, selected to meet the criterion $y^+ = yu_\tau/\nu \approx 1$ [37].

Figure 2 shows the features of the pitching motion. The sinusoidal pitching motion is defined as $\alpha = 10 + 15 \sin(\omega t)$, where α is the AOA and ω is the angular velocity, with the axis located $0.25c$ from the leading edge. In this numerical simulation, the reduced frequency $K = \omega c / (2U_\infty)$ was set as 0.05 or 0.1, as shown in Fig. 2b. The mean free stream velocity U_∞ was 14 m/s, and the turbulence intensity was set as 0.08%, corresponding to a Reynolds number of $Re =$

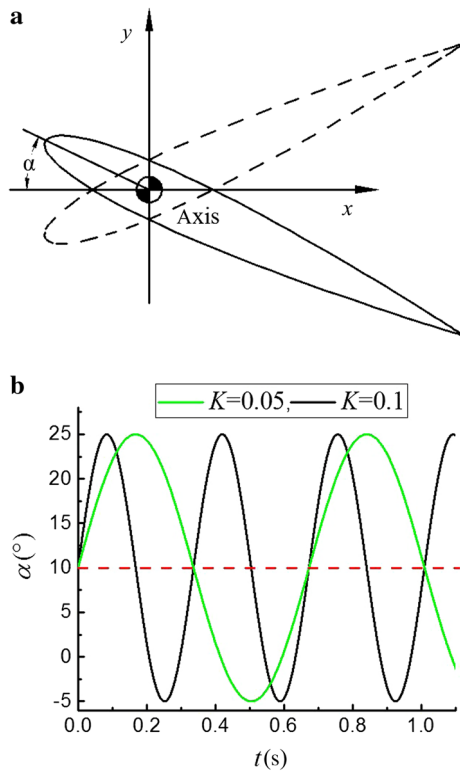


Fig. 2 Features of pitching airfoil motion: **a** pitching airfoil, **b** sinusoidal pitching motion

1.35×10^5 . For clarity, the upward stage of the oscillating cycle is denoted by α^+ and the downward stage by α^- .

3.2 Numerical verification

Experimental data were obtained from Ref. [20], acquired using closely spaced multiple hot-film sensor arrays. In addition, the surface pressure distribution, thermal filament wake measurement, and smoke flow visualization technology were obtained to supplement the thermal film data. According to Ref. [20], the hot line signal is sampled at 2 kHz. The surface pressure distribution is made up of 61 pressure joints, connected with seven quick-response micropressure sensors and distributed on the upper and lower surfaces of the model. With shutter speed of 1/1000 of a second, smoke flow visualization was carried out using a 60 Hz camera. A potentiometer was used to measure the instantaneous angle of attack of the wing with accuracy of 0.1° .

To obtain a grid- and time-independent solution, grid independence and temporal resolution validation were confirmed. Figure 3 shows the evolution of the lift coefficient $C_l = L/(0.5\rho U_\infty^2 sc)$ for the pitching foil with reduced frequency $K = 0.1$, where L and s are the lift and the span length, respectively, obtained using three sets of grid configurations with 9.1×10^4 , 2.2×10^5 , and 5.0×10^5 elements, with the time step chosen as 1×10^{-4} s. In the upward rotation

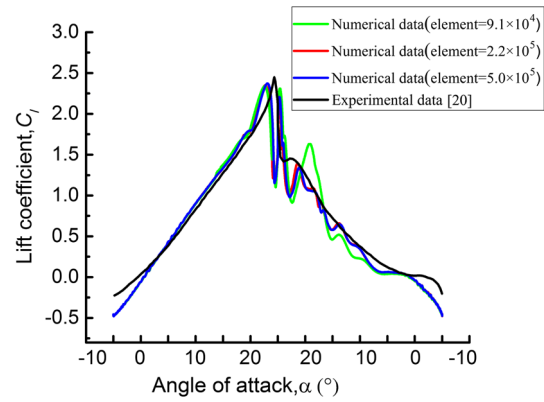


Fig. 3 Comparison of lift coefficient (C_l) predicted using different grid elements for reduced frequency $K = 0.1$, $Re = 135,000$, and $U_\infty = 14$ m/s

process ($\alpha^+ = -5^\circ - \alpha^+ = 25^\circ$), the predicted lift coefficient is approximately the same for all cases, increasing approximately linearly with the AOA. In the downward rotation process ($\alpha^+ = 25^\circ - \alpha^- = -5^\circ$), the numerical results obtained using 2.2×10^5 and 5.0×10^5 grid elements are approximately the same and agree well with the experiments. Considering computational efficiency, 2.2×10^5 elements were considered sufficient to yield grid independence.

To further analyze the uncertainty of the solution, grid convergence and numerical uncertainty were judged using the grid convergence index (GCI) method [44–49]. According to Ref. [50], the representative grid size h , grid refinement factor r , and apparent order p are defined as

$$h_i = \left[\frac{1}{N} \sum_{k=1}^N (\Delta A_k) \right]^{1/2}, \quad i = 1, 2, 3, \tag{10}$$

$$r_{ij} = h_i/h_j, \quad i, j = 1, 2, 3, \tag{11}$$

$$p = \frac{1}{\ln r_{21}} \left| \ln |\varepsilon_{32}/\varepsilon_{21}| + \ln \left[\frac{(r_{21}^p - 1) \text{sgn}(\varepsilon_{32}/\varepsilon_{21})}{(r_{32}^p - 1) \text{sgn}(\varepsilon_{32}/\varepsilon_{21})} \right] \right|, \tag{12}$$

where ΔA_k represents the k -th element, N is the total element number, $\varepsilon_{32} = f_3 - f_2$, $\varepsilon_{21} = f_2 - f_1$, f_i denotes the solution on the i -th grid, $r_{21} = h_2/h_1$, and $r_{32} = h_3/h_2$.

The approximate and extrapolated relative error are defined as

$$e_a^{21} = \left| \frac{f_1 - f_2}{f_1} \right|, \tag{13}$$

$$e_{\text{ext}}^{21} = \left| \frac{\frac{r_{21}^p f_1 - f_2}{r_{21}^p - 1} - f_1}{\frac{r_{21}^p f_1 - f_2}{r_{21}^p - 1}} \right|. \tag{14}$$

Table 1 Discretization error and uncertainties for numerical results

r_{21}	1.55
r_{32}	1.51
f_1	0.6744
f_2	0.6594
f_3	0.6622
p	3.7209
e_a^{21}	0.0222
e_{ext}^{21}	0.0054
GCI_{fine}^{21}	0.0067
GCI_{medium}^{32}	0.0352

The fine-grid convergence index is defined as

$$GCI_{fine}^{21} = \frac{1.25e_a^{21}}{r_{21}^p - 1}. \tag{15}$$

The averaged lift coefficient is considered to be an important parameter for analysis of dynamic performance and was therefore chosen as the main parameter for uncertainty analysis. The relative parameters were calculated and are presented in Table 1. Based on the error analysis results, the value of the GCI for the average lift coefficient was found to be 0.67% and 3.52%. As both uncertainty estimators lie in a reasonable range, the medium grid (2.2×10^5) was selected for all simulations in the present work.

Additionally, numerical results obtained using different time step sizes are presented in Fig. 4. Compared with the experimental data, the lift coefficient predicted with $\Delta t = 1 \times 10^{-3}$ s cannot reflect the transient lift evolution in the downstroke, while when the time step was chosen as $\Delta t = 1 \times 10^{-4}$ s or $\Delta t = 1 \times 10^{-5}$ s, the predicted lift coefficient remained almost the same. Hence, a time step of $\Delta t = 1 \times 10^{-4}$ s was chosen for the computations, ensuring a Courant number of $CFL_x = U_\infty \times \Delta t / \Delta x \approx 1$ in the streamwise direction and $CFL_y = V_\infty \times \Delta t / \Delta y \approx 1$ in the y -direction.

3.3 Extracted power and efficiency

Improved understanding of dynamic stall characteristics will help development of oscillating wing systems, which represent one of the primary flow energy conversion technologies, to enhance the energy harvesting performance for wind or hydro energy. Hence, the instantaneous power coefficient C_{Power} and the total energy extraction efficiency η were evaluated to quantify the energy extraction performance of the oscillating foil system, also representing a valuable reference for wind turbine blade designs. The instantaneous power extracted from the flow comes from the pitching contribution, and the energy extraction efficiency is defined as the ratio of

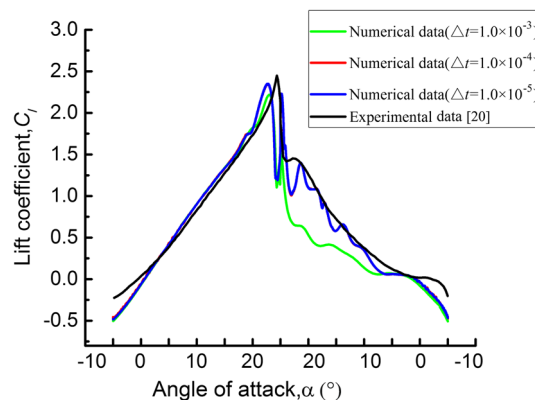


Fig. 4 Comparison of lift coefficient (C_l) predicted using different time step sizes for reduced frequency $K = 0.1$, $Re = 135,000$, and $U_\infty = 14$ m/s

the mean total power extracted to the total power available in the oncoming flow passing through the swept area.

To quantify the energy extraction performance of an oscillating foil system, the nondimensional power coefficient C_{Power} and the energy extraction efficiency η are defined as

$$C_{Power} = \frac{P_{Power}}{\frac{1}{2}\rho U_\infty^3 sc}, \tag{16}$$

$$P_{Power} = M(t) w_p(t), \tag{17}$$

$$\eta = \frac{\overline{P_{Power}}}{\frac{1}{2}\rho U_\infty^3 sd}, \tag{18}$$

$$\overline{P_{Power}} = \frac{1}{T} \int_0^T P_{Power}(t) dt, \tag{19}$$

where P_{Power} and $\overline{P_{Power}}$ are the instantaneous and time-averaged power, respectively, extracted from the oncoming flow from the pitching contribution, $M(t)$ is the torque about the pitching center, $w_p(t)$ is the transient angular velocity, d is the vertical extent of the oscillating foil, and T is the period of one pitching cycle.

4 Results and discussion

4.1 Analysis of transient aerodynamic load and flow features

Figure 5 shows the evolution of the lift coefficient C_l and drag coefficient C_d ($C_d = D / (0.5\rho U_\infty^2 sc)$, where D is the drag) with the AOA. The dynamic experimental results shown in Fig. 5 were obtained from Ref. [20]. It is shown that, in the upstroke from t_1 ($\alpha^+ = -5^\circ$) to t_7 ($\alpha^+ = 25^\circ$), the numerical results agree well with the experimental data, showing a maximum predicted C_l very close to the measured value. In the downstroke, the predicted lift coefficient presents small

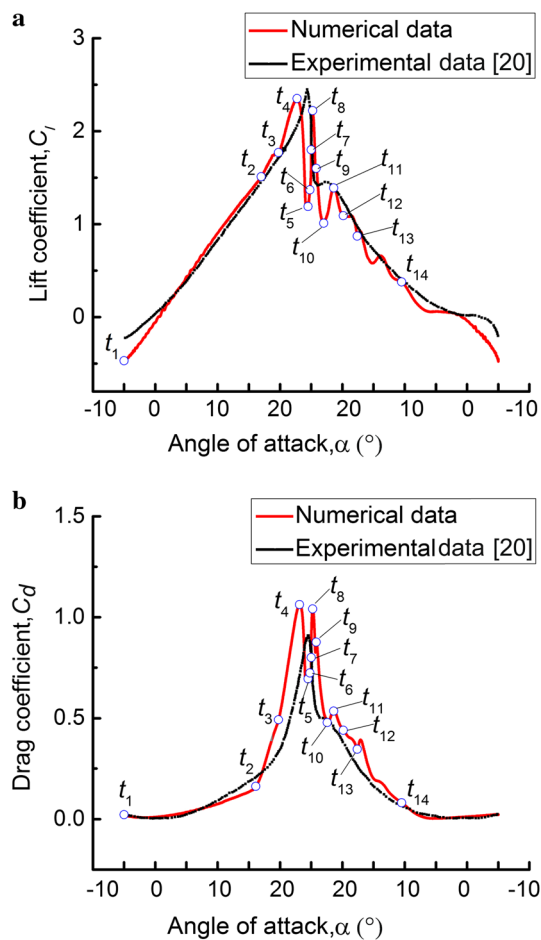


Fig. 5 Comparison of predicted **a** lift coefficient (C_l) and **b** drag coefficient (C_d) during the pitching process at reduced frequency $K = 0.1$ for $Re = 135,000$ and $U_\infty = 14$ m/s

amplitude and low-frequency oscillating behavior from t_7 ($\alpha^+ = 25^\circ$) to t_{13} ($\alpha^- = 18.1^\circ$). This may be due to the interaction between the induced secondary vortex on the leading and trailing edge; detailed analysis of the flow features is presented in the following paragraphs.

The z -vorticity contours at 14 representative times and the predicted pressure coefficients are presented in Figs. 6 and 7. For sinusoidal pitching motion, the evolution of the flow structures and the corresponding aerodynamic responses can be divided into three phases: (1) prior to dynamic stall, (2) dynamic stall, (3) poststall.

Prior to dynamic stall, the flow is fully attached to the foil and the flow structure is quasisteady and laminar from t_1 ($\alpha^+ = -5^\circ$) to t_2 ($\alpha^+ = 17.5^\circ$), as shown in Fig. 6a, b. The lift coefficient C_l increases almost linearly, and the drag coefficient C_d increases approximately as a quadratic function of AOA, as shown in Fig. 5. At t_2 ($\alpha^+ = 17.5^\circ$), the leading edge induces a vortex, as it is subject to severe pressure gradients, as shown in Figs. 6b and 7. The first LEV extends to approximately a semichord position of the suction side,

accompanied by a low-pressure region at t_3 ($\alpha^+ = 20.4^\circ$), as shown in Figs. 6c and 7, which is responsible for the sudden increase of the lift and drag coefficients. Until t_4 ($\alpha^+ = 23.5^\circ$), the first LEV covers the entire suction surface, as shown in Fig. 6d, and the corresponding lift and drag coefficients approach their maximum.

During dynamic stall, at t_5 ($\alpha^+ = 24.4^\circ$), the first trailing-edge vortex (TEV) forms. Meanwhile, the first LEV is detaching from the suction surface due to the interplay between the first leading and trailing vortices, resulting in the sudden reduction of the lift and drag coefficients. Meanwhile, the leading edge develops a secondary vortex at the same time, as shown in Fig. 6e, named the secondary LEV. When the AOA reaches $\alpha^+ = 24.8^\circ$ (t_6), the secondary LEV extends to one-third chord of the suction side, accompanied by a low-pressure region, as shown in Figs. 6f and 7. At the same time, the lift and drag coefficients increase again. Then, from t_7 ($\alpha^+ = 25^\circ$) to t_8 ($\alpha^- = 24.7^\circ$), the development and attachment of the secondary LEV, as well as the shedding of the first TEV, can be observed again, which corresponds to C_l and C_d approaching another peak value, as shown in Figs. 5 and 6g, h. However, this peak value is lower than the maximum value observed at t_4 ($\alpha^+ = 23.5^\circ$). At t_9 ($\alpha^- = 24.2^\circ$), the secondary TEV forms and begins to extrude the secondary LEV, as shown in Fig. 6i. When the AOA reaches $\alpha^- = 22.8^\circ$ (t_{10}), the secondary LEV sheds away, resulting in a reduction of the slope of the lift and drag coefficient curves, as shown in Figs. 5 and 6j.

During the poststall, the severe pressure gradient decreases at t_{11} ($\alpha^- = 21.8^\circ$), and the suction surface forms a merged vortex instead of the attached LEV, as shown in Figs. 6k and 7. At the same time, the secondary TEV has shed away. As α decreases, formation and shedding of a third TEV occur from t_{12} ($\alpha^- = 19.8^\circ$) to t_{13} ($\alpha^- = 18.1^\circ$). The interaction between the merged vortex and the third TEV results in small-amplitude oscillation of the lift and drag coefficients, as shown in Figs. 5 and 6l, m. When the angle of attack reaches t_{14} ($\alpha^- = 10.5^\circ$), the flow begins to transit from turbulent to laminar, as shown in Fig. 6n, which causes the dynamic forces to drop gently.

In summary, the z -vorticity can be used to capture the evolution of the vortex structures in the transient flow field, and the extremum values of the z -vorticity represent the centers of circulation regions. However, a region of high vorticity (ω_z) is not necessarily a vortex, as the shear flow near the wall can also experience high shear. As shown in Fig. 6f, at t_6 ($\alpha^+ = 24.8^\circ$), the approximate center position of the suction face has high vorticity, but not a real vortex according to the instantaneous streamlines. Hence, there are some limitations in using the z -vorticity ω_z to distinguish between vorticity due to a vortex or shear. To provide insight into the vortex structures during the dynamic stall process, a new analytical method is applied in the next section.

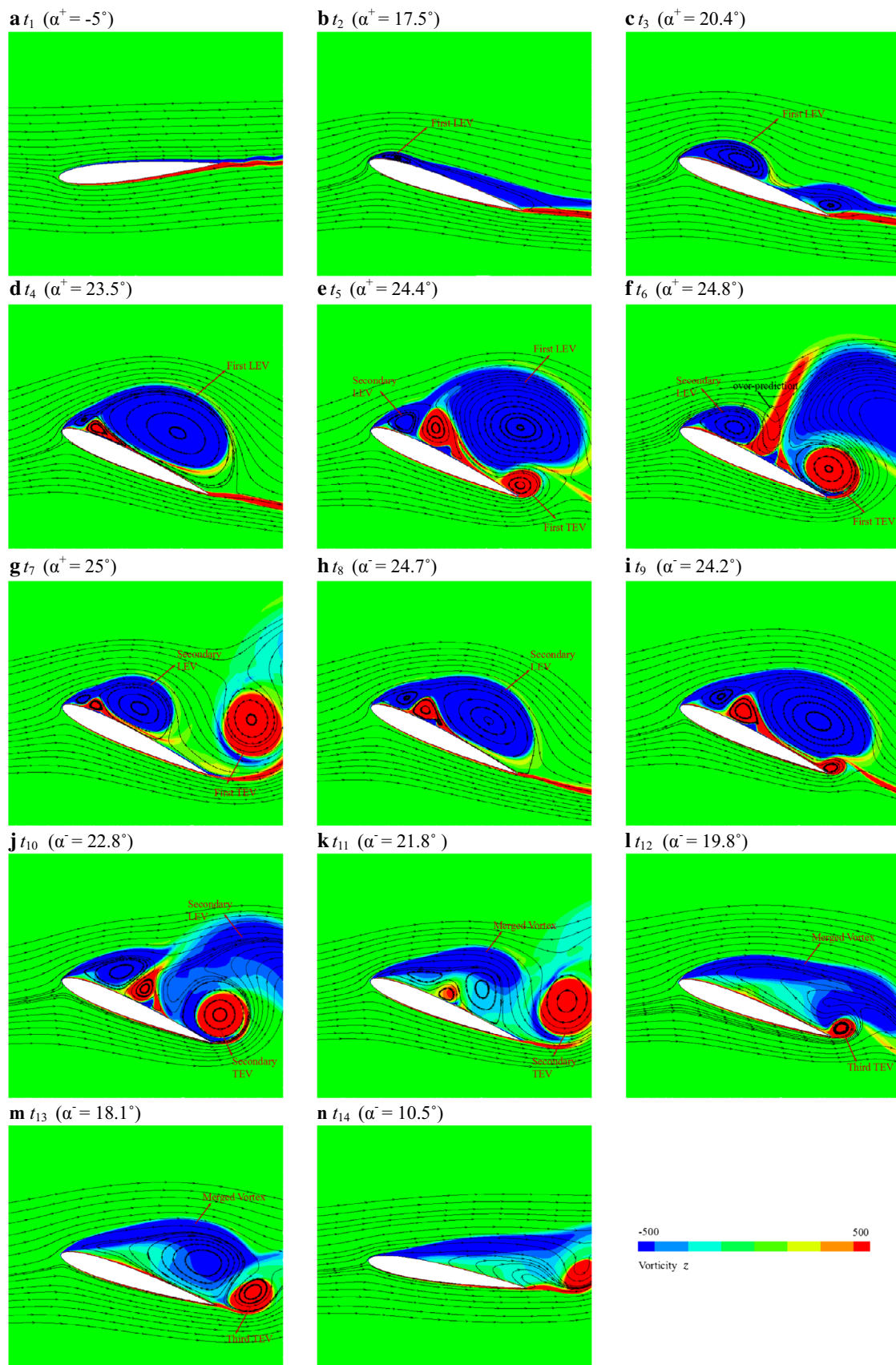


Fig. 6 Contours of z-vorticity superimposed on instantaneous streamlines at representative times ($K = 0.1$)

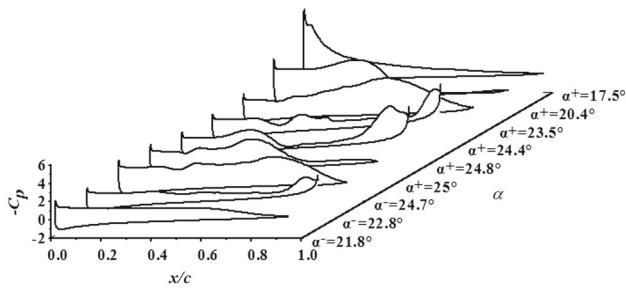


Fig. 7 Comparison of predicted pressure coefficients at representative times ($K = 0.1$)

4.2 Lagrangian-based analysis of flow structures in the dynamic stall process

As the dynamic stall process plays a significant role in energy capture by a wind turbine system, in this section, further analysis of the flow structures using the particle-based Lagrangian approach is presented, with focus on the dynamic stall process from t_2 ($\alpha^+ = 17.5^\circ$) to t_{11} ($\alpha^- = 21.8^\circ$). According to the evolution of the LEV and TEV, the process from t_2 ($\alpha^+ = 17.5^\circ$) to t_{11} ($\alpha^- = 21.8^\circ$) can be divided into two phases: (1) prior to dynamic stall stage, (2) dynamic stall stage.

(1) Prior to dynamic stall stage ($\alpha^+ = 17.5^\circ$ – 23.5°)

In Fig. 8, the FTLE field and corresponding LCS at t_2 ($\alpha^+ = 17.5^\circ$), t_3 ($\alpha^+ = 20.4^\circ$), and t_4 ($\alpha^+ = 23.5^\circ$) prior to the dynamic stall stage are presented. In this study, based on the velocity distribution in the flow field, the displacement of each particle can be calculated from an integral of the velocity, then the particle trajectory can be obtained during the time interval $T_{LE} = 0.005$ s (50 numerical steps). The ridges of the FTLE field, LCSs, are used to define the boundary of the vortex structures accurately. The LCSs can be categorized as LCS A and LCS B in Fig. 8a, indicating the flow region outside and inside the leading-edge vortex region, respectively. The pink particle inside LCS A exhibits a clockwise trajectory during the time interval $T_{LE} = 0.005$ s with low value of FTLE. The brown particle outside LCS A and the cyan particle inside LCS B move downstream due to the quasilinear flow during the time interval T_{LE} . As α increases, it should be noted that, at t_3 ($\alpha^+ = 20.4^\circ$), LCS A and LCS B become larger as the first LEV is growing. The cyan particle trajectory inside LCS B remains clockwise during the time interval T_{LE} , which corresponds to the evolution of the small vortex at the leading edge. In Fig. 8c, LCS A has covered the whole suction surface. At the same time, LCS C, LCS E, and LCS D are newly formed, representing

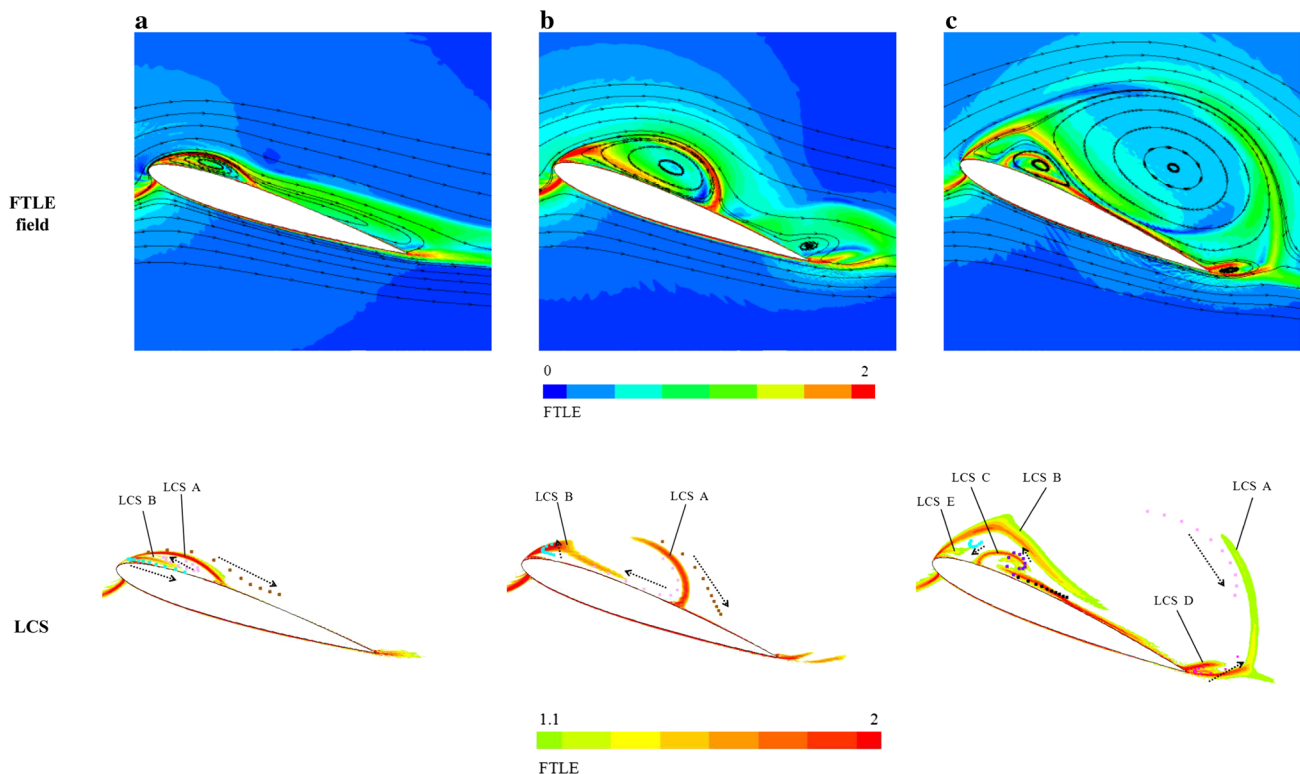


Fig. 8 FTLE field and corresponding LCS during LEV developments stage ($K = 0.1$): **a** t_2 ($\alpha^+ = 17.5^\circ$), **b** t_3 ($\alpha^+ = 20.4^\circ$), **c** t_4 ($\alpha^+ = 23.5^\circ$)

the boundary of leading-edge vortexes with reverse rotational direction and the first TEV. This can also be seen from the purple particle inside LCS C and the pink particle inside LCS D.

(2) Dynamic stall stage ($\alpha^+ = 23.5^\circ - \alpha^- = 21.8^\circ$)

To provide insight into the vortex structures in this stage, as shown in Fig. 9, the FTLE field and corresponding LCS at t_5 ($\alpha^+ = 24.4^\circ$), t_6 ($\alpha^+ = 24.8^\circ$), t_7 ($\alpha^+ = 25^\circ$), t_8 ($\alpha^- = 24.7^\circ$), t_{10} ($\alpha^- = 22.8^\circ$), and t_{11} ($\alpha^- = 21.8^\circ$) are presented. At t_5 ($\alpha^+ = 24.4^\circ$), LCS D rolls up and becomes larger in size with the development of the first TEV, accompanied by shedding of the first LEV. Meanwhile, LCS C forms outside LCS B, which results from shedding of the first LEV and the interaction between the reverse-directional vortex structures. During the time interval T_{LE} , the black and purple particles in Fig. 9a bypass the circulation region and follow its boundary. LCS B indicates the boundary of the secondary LEV. After the time interval T_{LE} , the green particle in Fig. 9a moves backward on the surface.

When it reaches t_6 ($\alpha^+ = 24.8^\circ$), LCS C becomes weaker. This means that the visibility of the vortex boundaries and the vortex strength become weaker. LCS D becomes larger and sheds away. LCS B and E also become larger and attached to the surface with the development of the secondary LEV. Meanwhile, LCS F is newly formed inside LCS E, as shown in Fig. 9b. At t_7 ($\alpha^+ = 25^\circ$), LCS B covers three-quarters of the suction surface. The track of the gray-brown particle inside LCS E indicates that the vortex center moves downstream. The blue particle inside LCS F rolls up and attaches at the surface due to the suction force of the secondary LEV. When the angle of attack reaches $\alpha^- = 24.7^\circ$ (t_8), LCS B has covered the whole suction surface with low-pressure region, as shown in Fig. 8, which leads to the secondary increase of the lift coefficient.

As α decreases in the downstroke phase, the secondary LEV sheds away and the secondary TEV is induced. At t_{10} ($\alpha^- = 22.8^\circ$), LCS G, which represents the boundary of the secondary TEV, extrudes LCS B, as shown in Fig. 9e. The gray-brown particle is attracted to leave the foil by the suction force. Because of the interaction of the secondary LEV and TEV, the blue and cyan particles are forced to attach to the surface. This results in a decline of the lift coefficient again. When it reaches t_{11} ($\alpha^- = 21.8^\circ$), LCSs weaken gradually. As α decreases, LCS F constantly merges with the free stream flow and sheds away on account of the interaction between the merged vortex and the third TEV, which is responsible for the small-amplitude oscillating behavior in the lift and drag coefficient curves.

4.3 Influence of reduced frequency on flow structures in dynamic stall process

To further investigate the effect of the oscillation frequency on the aerodynamic performance, the transient flow structures and corresponding aerodynamic characteristics at different reduced oscillating frequencies are discussed in this section.

Figures 10 and 11 show the evolution of the predicted lift coefficient (C_l) and power coefficient (C_{Power}) for different reduced frequencies ($K = 0.05$ and 0.1). Table 2 presents the energy extraction efficiency at the different reduced frequencies. It can be observed that the total energy extraction efficiency at $K = 0.1$ was larger than the case of $K = 0.05$. The z -vorticity contours and the instantaneous streamlines at typical angles of attack for both cases are shown in Fig. 12, where $t_1 - t_7$ represent typical times for the case with $K = 0.1$ and $t'_1 - t'_7$ for the case with $K = 0.05$. Comparisons of the predicted pressure coefficients for the cases with different reduced frequencies ($K = 0.05$ and 0.1) are shown in Fig. 13.

Prior to dynamic stall, it is found that the evolution of the predicted C_l and the power coefficient (C_{Power}) are similar for the different reduced frequencies, as shown in Figs. 10 and 11. The corresponding C_l increases almost linearly with increasing angle, while the corresponding C_{Power} remains at low amplitude then increases sharply. At $K = 0.05$, the formation of the first LEV occurs at t_1 ($\alpha^+ = 16^\circ$), being more specific than at $K = 0.1$, as shown in Fig. 12a, g. The larger adverse pressure gradient distributions at $\alpha^+ = 16^\circ$ for $K = 0.05$ are responsible for the advanced formation of the first LEV, as shown in Fig. 13a. The first LEV begins to develop with the low-pressure region at t'_2 ($\alpha^+ = 17.1^\circ$), resulting in the sharp increase of C_l and C_{Power} , as shown in Figs. 10 and 11. When it reaches t'_3 ($\alpha^+ = 19.5^\circ$), the first LEV has developed and covered the entire suction surface, as shown in Fig. 12b, c. As α increases, the low-pressure region moves to the trailing edge with the development of the first LEV, significantly enhancing the lift and power prior to the dynamic stall process. The adverse pressure gradient distributions at the same angle are larger for $K = 0.05$ than $K = 0.1$, as shown in Fig. 13a–c. This is because the pitching velocity is slow at $K = 0.05$, and the formation of the first LEV can develop adequately.

During dynamic stall, the stall point is again more specific and the maximum value of C_l and C_{Power} becomes low for $K = 0.05$, as shown in Figs. 10 and 11. This significantly affects the total energy extraction efficiency of the oscillating foil. With increase of the angle of attack, as shown in Fig. 13d, e, the adverse pressure gradient distributions at the suction surface for $K = 0.05$ become low with low variations instead of the complex pressure coef-

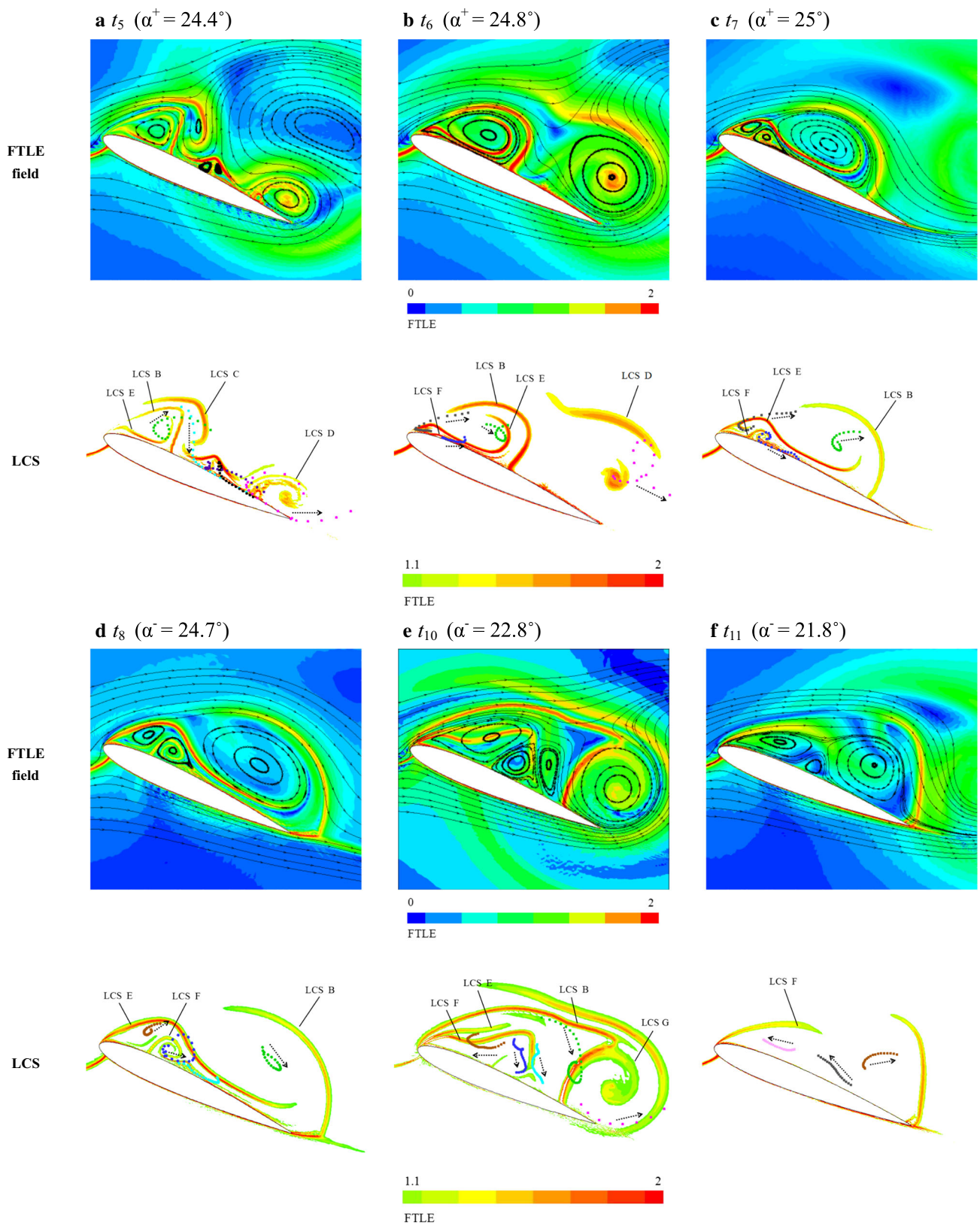


Fig. 9 FTLE field and corresponding LCS during poststall vortex shedding stage ($K = 0.1$)

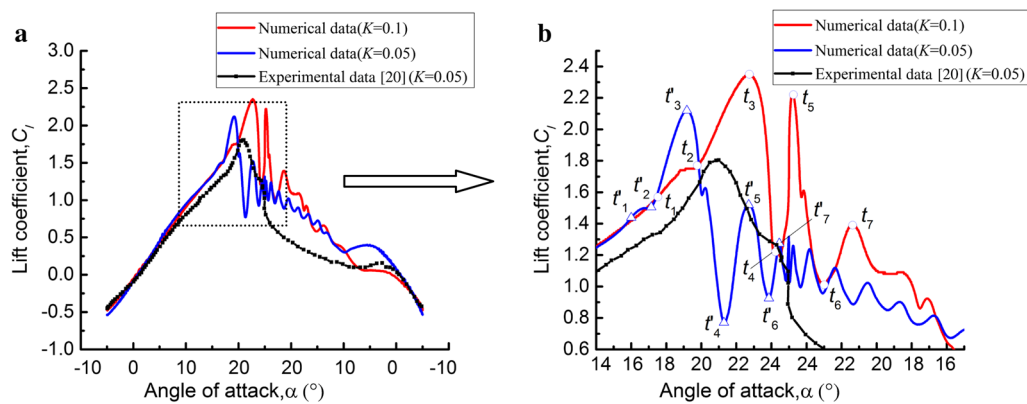


Fig. 10 Evolution of predicted C_l with different reduced frequencies ($K = 0.05$ and 0.1) for $Re = 135,000$: **a** full range, **b** zoomed view of dynamic stall process

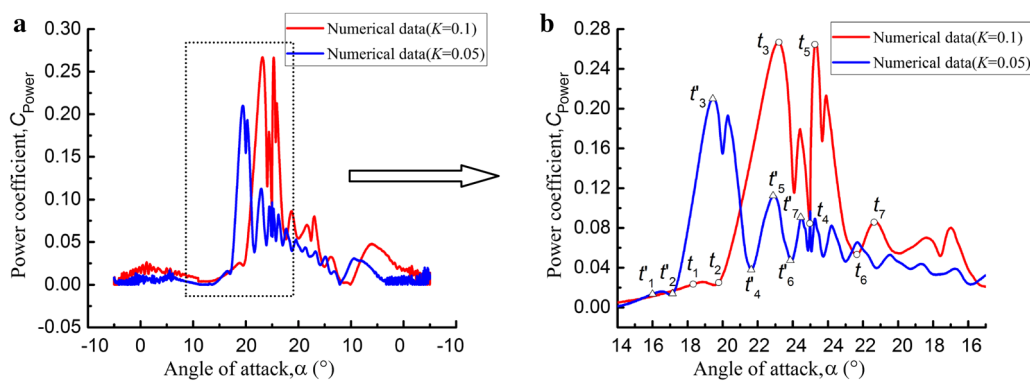


Fig. 11 Evolution of power coefficient (C_{Power}) with different reduced frequencies ($K = 0.05$ and 0.1) for $Re = 135,000$: **a** full range, **b** zoomed view of dynamic stall process

efficient distributions at $K = 0.1$. At t'_4 ($\alpha^+ = 21.7^\circ$) in the upstroke phase, the first LEV has already shed away and three vortices align alongside the upper surface compared with t_4 ($\alpha^+ = 24.4^\circ$), which is responsible for the decline of C_l and C_{Power} , as shown in Figs. 10, 11, and 12d. Compared with $K = 0.1$, the small-amplitude oscillating behavior becomes more severe for the case with $K = 0.05$ from t'_5 ($\alpha^+ = 23^\circ$), as shown in Figs. 10 and 11. Moreover, C_l and adverse pressure gradient distributions are lower than at $K = 0.1$, as shown in Figs. 10 and 13g, h. At t'_5 ($\alpha^+ = 23^\circ$), the vortex near the center clearly shrinks while another pair of vortices merge, as shown in Fig. 12e, which is responsible for the increase of C_l again. However, compared with the formation of the attached secondary LEV at t_5 ($\alpha^- = 24.7^\circ$), the merged vortex interacts with the secondary TEV at $K = 0.05$. It can be observed that no attached secondary LEV was induced at $K = 0.05$. This is responsible for the difference in the adverse pressure gradient distributions for different reduced frequencies, as shown in Fig. 13e–g. At t'_6 ($\alpha^+ = 24^\circ$), development and shedding of the secondary TEV result in the decline of C_l and C_{Power} 10 and 12f. In

Table 2 Energy extraction efficiency at different reduced frequencies ($K = 0.05$ and 0.1)

K	0.05	0.1
η (%)	32.18	55.46

the dynamic stall process, the evolution of the dynamic performance further results in a decrease of the total energy extraction efficiency compared with the case of $K = 0.1$. When the angle of attack increases to t'_7 ($\alpha^+ = 24.5^\circ$), the third TEV is induced on the trailing edge, as shown in Fig. 12f. As α declines in the downstroke phase, TEV formation, interaction, and shedding are repeated many times, being responsible for the decreasing amplitude and high-frequency oscillating behavior of the flow. This is mainly attributed to the merged vortex and TEV having sufficient time to develop and interact for $K = 0.05$. This oscillating behavior may result in the decrease of the total energy extraction efficiency of the oscillating foil. For $K = 0.1$, the pitching velocity is too fast for the vortex to develop and interact completely.

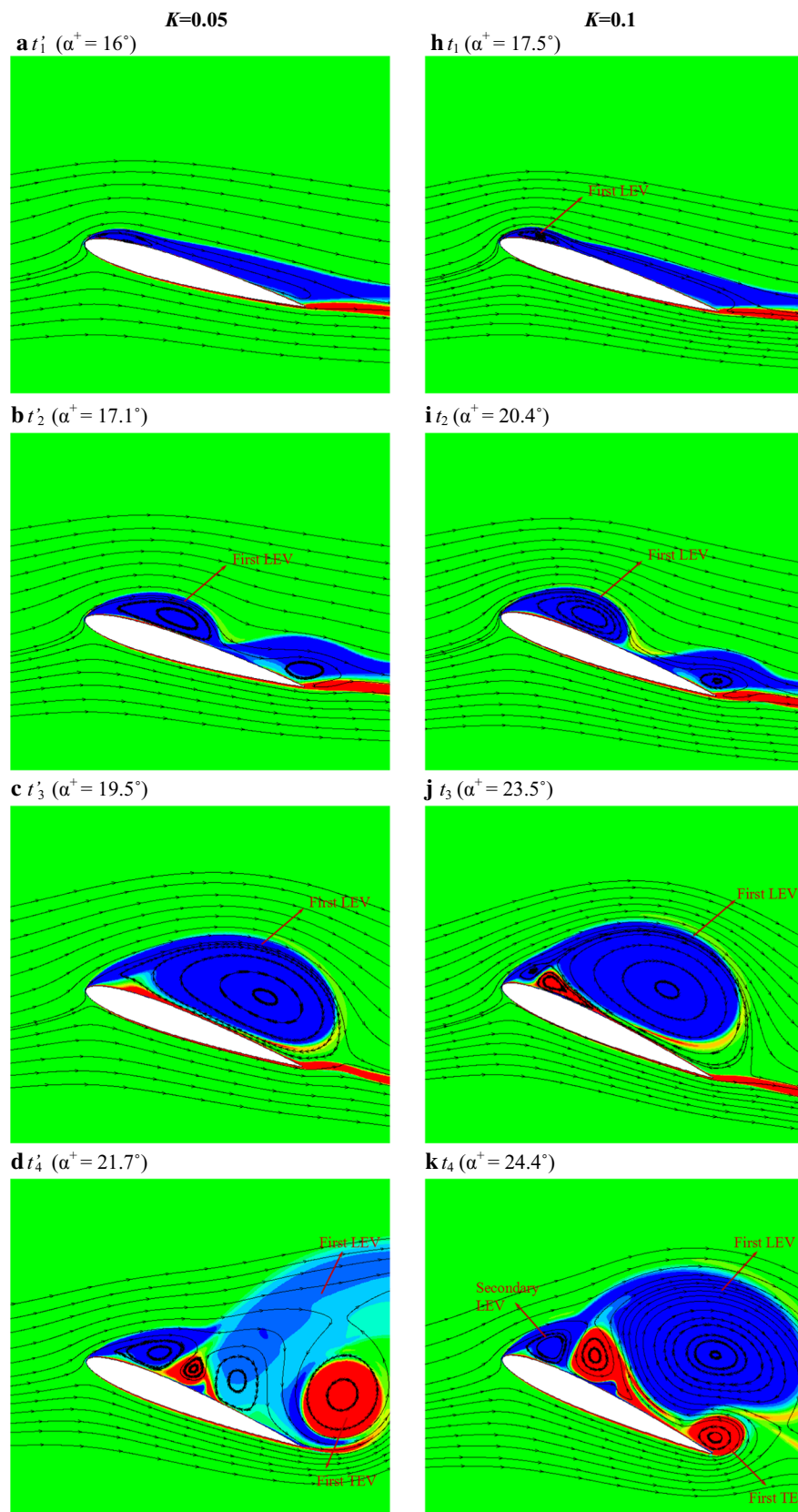


Fig. 12 Contours of z -vorticity superimposed on instantaneous streamlines at different angles of attack ($K = 0.05$ and 0.1)

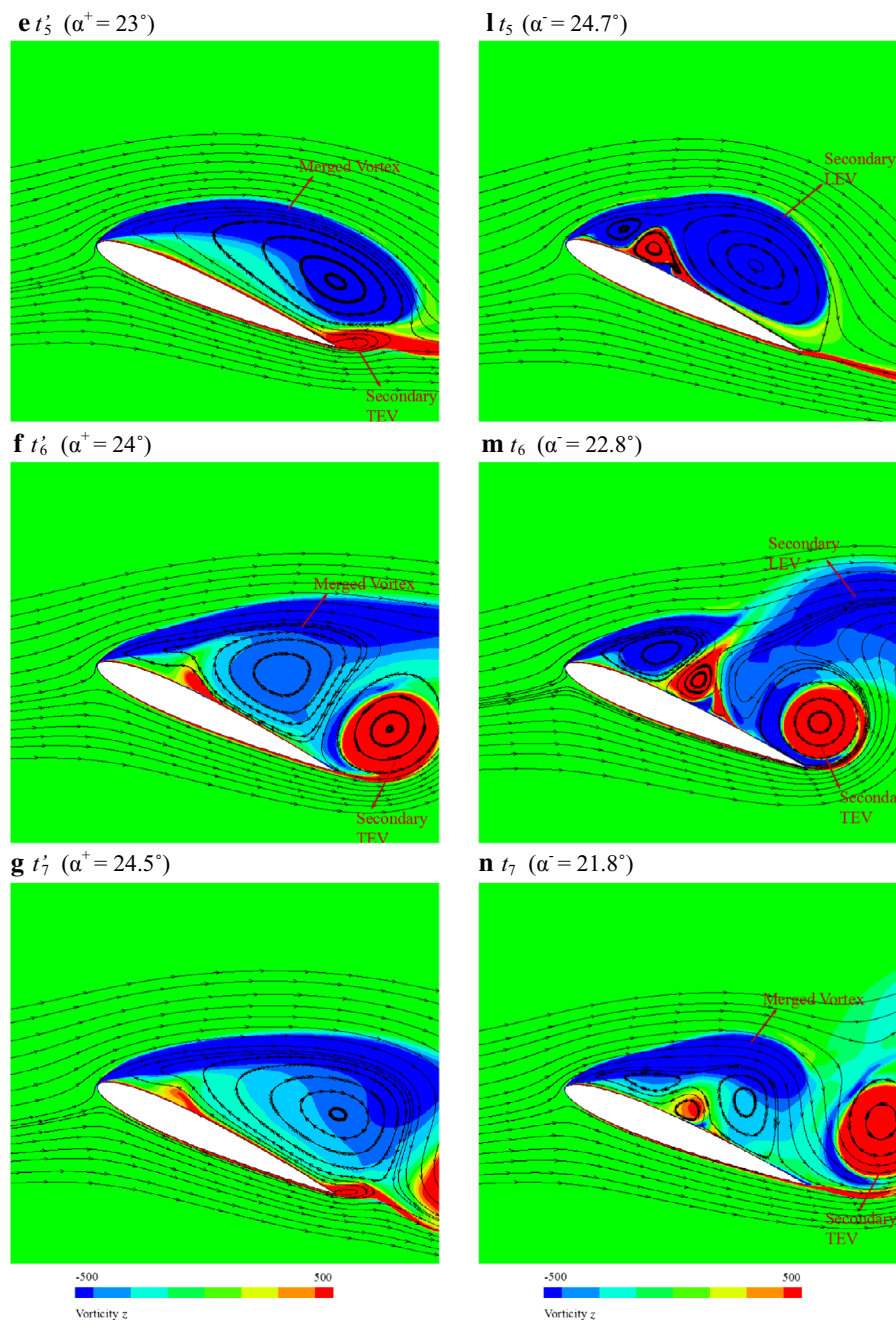


Fig. 12 continued

5 Conclusions

The coupled $k-\omega$ SST turbulence model and $\gamma-Re_\theta$ transition model were used to simulate the dynamic stall phenomenon for an oscillating NACA0012 airfoil. The numerical results were validated by comparison with experimental results. The main conclusions are as follows:

- (1) During dynamic stall, the first LEV is forced to shed away due to the strong interaction between the first

leading- and trailing-edge vortex, which is responsible for the reduction of the lift and drag coefficients. With increase of the angle of attack, the secondary LEV repeats this formation, interaction, and shedding process, leading to a secondary rise and fall of the lift and drag coefficients. During poststall, the leading edge of the suction surface forms a merged vortex, which interacts with the TEV, corresponding to large-scale low-frequency load fluctuations. Meanwhile, the LCSs gradually fade away with shedding of the merged vortex.

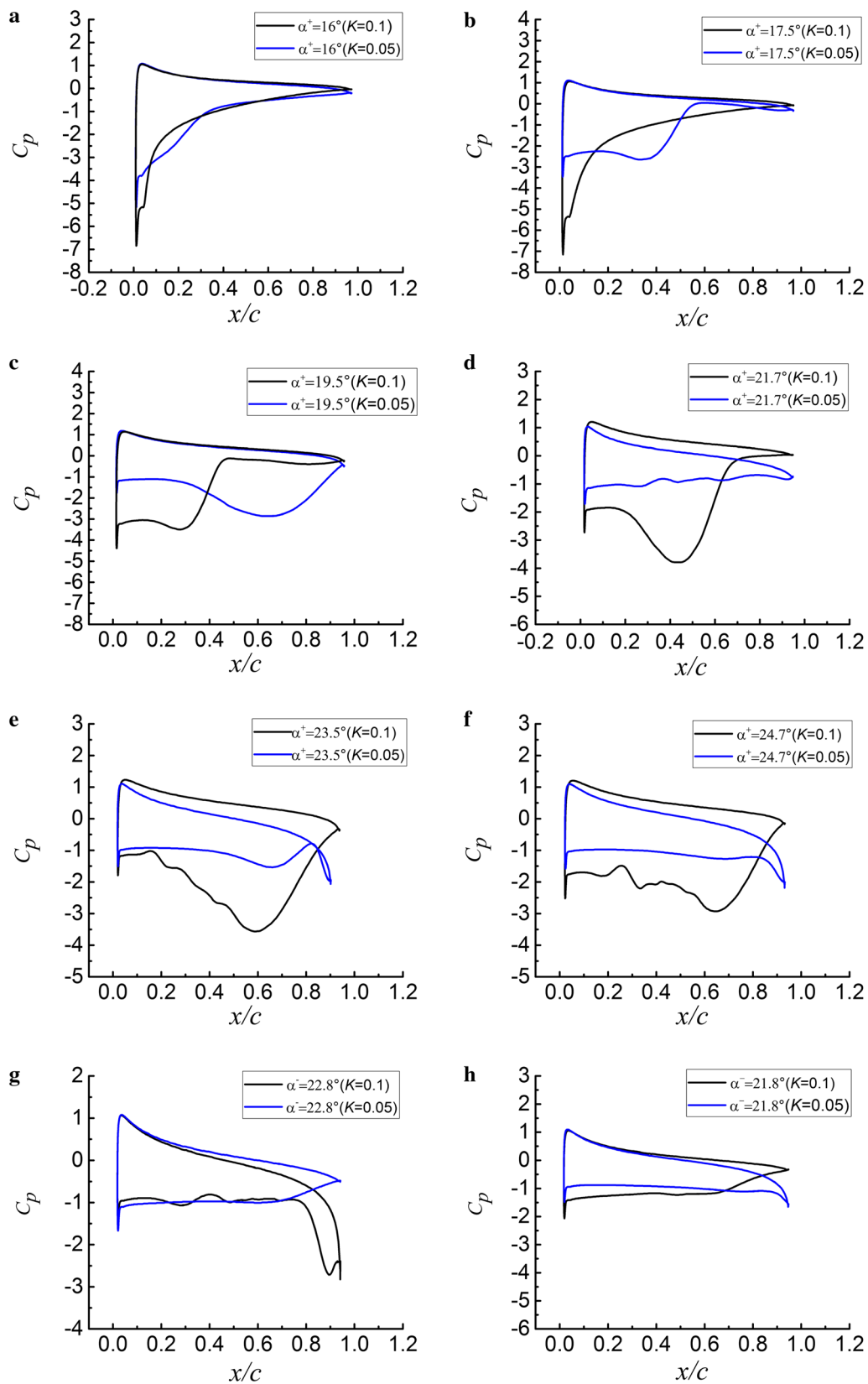


Fig. 13 Comparisons of predicted pressure coefficients at same geometric angles of attack for different reduced frequencies ($K = 0.05$ and 0.1)

- (2) The reduced frequency significantly affects the flow structures and energy extraction performance in the dynamic stall process. At $K = 0.1$ and 0.05 , the evolution of C_l and C_{Power} is approximately similar prior to the dynamic stall process. However, compared with the case of $K = 0.1$, the dynamic stall point is advanced and no attached secondary LEV is generated when $K = 0.05$. Additionally, the small-amplitude oscillating behavior of the dynamic curve becomes more severe for the case of $K = 0.05$. These phenomena result in the oscillating behavior of the power coefficient (C_{Power}) and affect the total energy extraction efficiency. The total energy extraction efficiency is higher for $K = 0.1$ than $K = 0.05$.
- (3) LCSs defined by ridges of the FTLE field were utilized to investigate transient flow structures. Compared with the Eulerian approach, e.g., using the z -vorticity (ω_z), such Lagrangian-based analysis of flow structures in the dynamic stall process can effectively avoid overprediction of vortex structures. The dynamic behavior of the flow structures was effectively identified using the FTLE field.

In the future, the three-dimensional effect [51–54] and its interactions with turbulence and energy harvesting are worthy of further investigation, so LCS and particle tracking techniques will be applied to three-dimensional flow fields to present more details of the transient flow structures. To determine the spatial and temporal variation of the turbulent structures more accurately, direct numerical simulations (DNS) and large-eddy simulations (LES) will be added in future work. In addition, the effect of the pitching amplitude on the flow evolution and energy harvesting performance will also be discussed further in the future.

Acknowledgements This work was supported by the National Postdoctoral Program for Innovative Talents (Grant BX201700126), the China Postdoctoral Science Foundation (Grant 2017M620043), the National Natural Science Foundation of China (Grants 51679005 and 91752105), and the National Natural Science Foundation of Beijing (Grant 3172029).

References

- Melício, R., Mendes, V.M.F., Catalão, J.P.S.: Transient analysis of variable-speed wind turbines at wind speed disturbances and a pitch control malfunction. *Appl. Energy* **88**, 1322–1330 (2011)
- González, L.G., Figueres, E., Garcerá, G., et al.: Maximum-power-point tracking with reduced mechanical stress applied to wind-energy-conversion-systems. *Appl. Energy* **87**, 2304–2312 (2010)
- Karbasian, H.R., Esfahani, J.A., Barati, E.: The power extraction by flapping foil hydrokinetic turbine in swing arm mode. *Renew. Energy* **88**, 130–142 (2016)
- Hang, L., Zhou, D., Lu, J., et al.: The impact of pitch motion of a platform on the aerodynamic performance of a floating vertical axis wind turbine. *Energy* **119**, 369–383 (2017)
- Mckenna, R., Leye, P.O.V.D., Fichtner, W.: Key challenges and prospects for large wind turbines. *Renew. Sustain. Energy Rev.* **53**, 1212–1221 (2016)
- Lu, K., Xie, Y., Zhang, D., et al.: Systematic investigation of the flow evolution and energy extraction performance of a flapping-airfoil power generator. *Energy* **89**, 138–147 (2015)
- Huang, B., Wu, Q., Wang, G.Y.: Numerical simulation of unsteady cavitating flows around a transient pitching hydrofoil. *Sci. China Technol. Sci.* **57**, 101–116 (2014)
- Lee, T.: Effect of flap motion on unsteady aerodynamic loads. *J. Aircr.* **44**, 334–338 (2015)
- Birch, D.M., Lee, T.: Tip vortex behind a wing undergoing deep-stall oscillation. *AIAA J.* **43**, 2081–2092 (2015)
- Liu, T.T., Huang, B., Wang, G.Y., et al.: Experimental investigation of the flow pattern for ventilated partial cavitating flows with effect of Froude number and gas entrainment. *Ocean Eng.* **129**, 343–351 (2017)
- Wang, Y.W., Xu, C., Wu, X.C., et al.: Ventilated cloud cavitating flow around a blunt body close to the free surface. *Phys. Rev. Fluids* **2**, 084303 (2017)
- Long, X.P., Cheng, H.Y., Ji, B., et al.: Large eddy simulation and Euler–Lagrangian coupling investigation of the transient cavitating turbulent flow around a twisted hydrofoil. *Int. J. Multiph. Flow* **100**, 41–56 (2018)
- Wang, G.Y., Wu, Q., Huang, B.: Dynamics of cavitation–structure interaction. *Acta Mech. Sin.* **33**, 685–708 (2017)
- Huang, B., Zhao, Y., Wang, G.Y.: Large eddy simulation of turbulent vortex-cavitation interactions in transient sheet/cloud cavitating flows. *Comput. Fluids* **92**, 113–124 (2014)
- Choudhry, A., Arjomandi, M., Kelso, R.: Methods to control dynamic stall for wind turbine applications. *Renew. Energy* **86**, 26–37 (2016)
- Hameed, M.S., Afaq, S.K.: Design and analysis of a straight bladed vertical axis wind turbine blade using analytical and numerical techniques. *Ocean Eng.* **57**, 248–255 (2013)
- Huang, B., Young, Y.L., Wang, G.Y., et al.: Combined experimental and computational investigation of unsteady structure of sheet/cloud cavitation. *J. Fluids Eng. Trans. ASME* **135**, 071301 (2013)
- Ferreira, C.S., Bussel, G.V., Kuik, G.V.: 2D CFD simulation of dynamic stall on a vertical axis wind turbine: verification and validation with PIV measurements. In: 45th AIAA Aerospace Sciences Meeting and Exhibit (2006)
- Wernert, P., Geissler, W., Raffel, M., et al.: Experimental and numerical investigations of dynamic stall on a pitching airfoil. *AIAA J.* **34**, 982–989 (1996)
- Lee, T., Gerontakos, P.: Investigation of flow over an oscillating airfoil. *J. Fluid Mech.* **512**, 313–341 (2004)
- Carr, L.W.: Progress in analysis and prediction of dynamic stall. *J. Aircr.* **25**, 6–17 (1988)
- Ekaterinaris, J.A., Platzer, M.F.: Computational prediction of airfoil dynamic stall. *Prog. Aerosp. Sci.* **33**, 759–846 (1997)
- Simpson, B.J., Hover, F.S., Triantafyllou, M.S.: Experiments in direct energy extraction through flapping foils. in: the Eighteenth International Offshore and Polar Engineering Conference, 2008
- Shehata, A.S., Xiao, Q., Saqr, K.M., et al.: Passive flow control for aerodynamic performance enhancement of airfoil with its application in wells turbine—under oscillating flow condition. *Ocean Eng.* **136**, 31–53 (2017)
- Tseng, C.C., Hu, H.A.: Dynamic behaviors of the flow past a pitching foil based on Eulerian and Lagrangian viewpoints. *AIAA J.* **54**, 712–727 (2016)

26. Ducoin, A., Astolfi, J.A., Deniset, F., et al.: Computational and experimental investigation of flow over a transient pitching hydrofoil. *Eur. J. Mech. B Fluids* **28**, 728–743 (2009)
27. Bhat, S.S., Govardhan, R.N.: Stall flutter of NACA 0012 airfoil at low Reynolds numbers. *J. Fluids Struct.* **41**, 166–174 (2013)
28. Wang, S., Ingham, D.B., Ma, L., et al.: Numerical investigations on dynamic stall of low Reynolds number flow around oscillating airfoils. *Comput. Fluids* **39**, 1529–1541 (2010)
29. Huang, B., Ducoin, A., Young, L.Y.: Physical and numerical investigation of cavitating flows around a pitching hydrofoil. *Phys. Fluids* **25**, 102109 (2013)
30. Chen, Y.L., Zhan, J.P., Wu, J., et al.: A fully-activated flapping foil in wind gust: energy harvesting performance investigation. *Ocean Eng.* **138**, 112–122 (2017)
31. Teng, L., Deng, J., Pan, D., et al.: Effects of non-sinusoidal pitching motion on energy extraction performance of a semi-active flapping foil. *Renew. Energy* **85**, 810–818 (2016)
32. Lai, J.C.S., Platzer, M.F.: Jet characteristics of a plunging airfoil. *AIAA J.* **37**, 1529–1537 (2015)
33. Gharali, K., Johnson, D.A.: Dynamic stall simulation of a pitching airfoil under unsteady freestream velocity. *J. Fluids Struct.* **42**, 228–244 (2013)
34. Guo, Q., Zhou, L., Wang, Z.: Comparison of BEM-CFD and full rotor geometry simulations for the performance and flow field of a marine current turbine. *Renew. Energy* **75**, 640–648 (2015)
35. Wu, Q., Wang, Y.N., Wang, G.Y.: Experimental investigation of cavitating flow-induced vibration of hydrofoils. *Ocean Eng.* **144**, 50–60 (2017)
36. Wu, Q., Huang, B., Wang, G.Y., et al.: Experimental and numerical investigation of hydroelastic response of a flexible hydrofoil in cavitating flow. *Int. J. Multiph. Flow* **74**, 19–33 (2015)
37. Menter, F.R.: Improved two-equation $k - \omega$ turbulence models for aerodynamic flows. *NASA Tech. Memo.* **34**, 103975 (1992)
38. Langtry, R.B., Menter, F.R., Likki, S.R., et al.: A correlation-based transition model using local variables-part I: model formulation. *J. Turbomach.* **128**, 413–422 (2006)
39. Langtry, R.B., Menter, F.R., Likki, S.R., et al.: A correlation-based transition model using local variables-part II: test cases and industrial applications. *J. Turbomach.* **128**, 423–434 (2006)
40. Menter, F.R., Langtry, R.B., Völker, S.: Transition modeling for general purpose CFD codes. *Flow Turbul. Combust.* **77**, 277–303 (2006)
41. Haller, G., Yuan, G.: Lagrangian coherent structures and mixing in two-dimensional turbulence. *Phys. D* **147**, 352–370 (2000)
42. Wu, Q., Huang, B., Wang, G.: Lagrangian-based investigation of the transient flow structures around a pitching hydrofoil. *Acta Mech. Sin.* **32**, 64–74 (2016)
43. Tseng, C.C., Liu, P.B.: Dynamic behaviors of the turbulent cavitating flows based on the Eulerian and Lagrangian viewpoints. *Int. J. Heat Mass Transf.* **102**, 479–500 (2016)
44. Wang, Z.Y., Huang, B., Zhang, M.D., et al.: Experimental and numerical investigation of ventilated cavitating flow structures with special emphasis on vortex shedding dynamics. *Int. J. Multiph. Flow* **98**, 79–95 (2018)
45. Roache, P.J.: Quantification of uncertainty in computational fluid dynamics. *Annu. Rev. Fluid Mech.* **29**, 123–160 (2003)
46. Gohil, P.P., Saini, R.P.: Effect of temperature, suction head and flow velocity on cavitation in a Francis turbine of small hydro power plant. *Energy* **93**, 613–624 (2015)
47. Roache, P.J.: Verification of codes and calculations. *AIAA J.* **36**, 696–702 (2012)
48. Kwasniewski, L.: Application of grid convergence index in FE computation. *Bull. Pol. Acad. Sci. Tech. Sci.* **61**, 123–128 (2013)
49. Kleinhans, M.G., Jagers, H.R.A., Mosselman, E., et al.: Procedure of estimation and reporting of uncertainty due to discretization in CFD applications. *J. Fluids Eng.* **130**, 078001 (2008)
50. Hunt, J.C.R., Wray, A.A., Moin, P.: Eddies, stream, and convergence zones in turbulent flows. Center for Turbulence Research Report CTR-S88. pp. 193–208 (1988)
51. Choudhry, A., Leknys, R., Arjomandi, M., et al.: An insight into the dynamic stall lift characteristics. *Exp. Therm. Fluid Sci.* **58**, 188–208 (2014)
52. Martinat, G., Braza, M., Hoarau, Y., et al.: Turbulence modeling of the flow past a pitching NACA0012 airfoil at 105 and 106 Reynolds numbers. *J. Fluids Struct.* **24**, 1294–1303 (2008)
53. Velkova, C., Todorov, M., Dobrev, I., et al.: Approach for numerical modeling of airfoil dynamic stall. in: *Proceedings of BulTrans-2012*, 26–28 September, Sozopol, 1–6 (2012)
54. Tseng, C.C., Cheng, Y.E.: Numerical investigations of the vortex interactions for a flow over a pitching foil at different stages. *J. Fluids Struct.* **58**, 291–318 (2015)